Received: 1 October 2019 | Revised: 13 December 2019 | Accepted: 10 January 2020

DOI: 10.1002/aic.16915

TRANSPORT PHENOMENA AND FLUID MECHANICS

AIChE JOURNAL

The permeability of replicated microcellular structures in the Darcy regime

Abdulrazak J. Otaru

Department of Chemical Engineering, Federal University of Technology, Minna, Niger State, Nigeria

Correspondence
Abdulrazak J. Otaru, Department of Chemical Engineering, Federal University of Technology, P.M.B. 065, Gidan-Kwanu Campus, Bida Road, Minna, Niger State, Nigeria.
Email: otaru_12257@yahoo.com

Abstract

This study provides an extension to previously published articles on measurements and computational fluid dynamic (CFD) modeling and simulations of airflow across "bottleneck-type" structures in the Forchheimer regime to purely inertial-neglected (Darcy regime) incompressible flowing fluid via tomography datasets. A linear-dependent relationship between the CFD computed unit pressure drop developed across the samples and the superficial fluid inlet velocity was observed for all the samples for creeping fluid flow ($0–7 \times 10^{-03}$ m·s^{-1}). The permeability of the structures was observed to be dependent on the structural parameters of the porous medium and most importantly, its pore diameter openings. Linear graphical relations between permeability and pore-structure related properties of these materials were observed and these could assist in minimizing the number of design iterations needed for the processing of self-supporting porous metals.

KEYWORDS

modeling, permeability, porous metals, simulation

1 | BACKGROUND

Man-made porous metallic structures such as steel, nickel, copper, aluminium, and alloys are characterized as sponge-like shaped cellular materials consisting of a metal frame (solid matrix), air-filled pores, and interconnecting pores, also known as "windows."[1-3] These interconnecting "windows" in cellular metals is considered[4] as an open volume within the metal matrix network that allows a uniform length of passages and distribution. They are classified into open-celled and close-celled cellular structures[5] and can be made by different technological processes like additive manufacturing, pressure-less sintering, replication-casting route, reactive processing, and gas entrapment techniques.[6,7] The resulting effects are a microstructural change aptly influenced by technological routes and operating conditions.[1,8,9] The unique and combined characteristics of lightweight, high surface area and high thermal conductivity of these materials enable their suitability as structures that interact with fluid and heat transfer processes. Typical examples of these processes are filters for high-temperature gas and fluid filtration, energy absorbers/package, heat exchangers, vibrational control, and mechanical damping.[10] Figure 1 presents a typical porous metallic structure made by replication casting routes of pouring liquid melts in the convergent gaps created by packed beds of monosized porogens. A detailed processing route adopting this technique is described in References 8, 9, 11-13.

Generally, the relationship between superficial fluid velocity (v_s) and the unit pressure drop (∇p) developed across porous metals in laminar and turbulent regimes are reportedly[14-16] described to obey the Darcy–Dupuit–Forchheimer second-order model given by Equation 1.

$$-\frac{\partial p}{\partial x_i} = \nabla p = \frac{\mu}{k_o} v_s + \rho C v_s^2 \text{ and } C = \frac{C_F}{\sqrt{k_o}} \quad (1)$$

where ∇p is pressure drop per unit flow thickness (Pa·m^{-1}), v_s is the superficial fluid velocity (m·s^{-1}), μ is the fluid dynamic viscosity (Pa·s), ρ is the fluid density (kg·m^{-3}), k_o is the permeability of the material (m^2), C is the Form drag (m^{-1}), C_F dimensionless Forchheimer coefficient, v_p is the pore fluid velocity, and ε is the pore volume fraction. For a very low fluid velocity, typified by pore diameter Reynolds (R_{ED}) number less than one, a viscous-drag energy dissipation mechanism

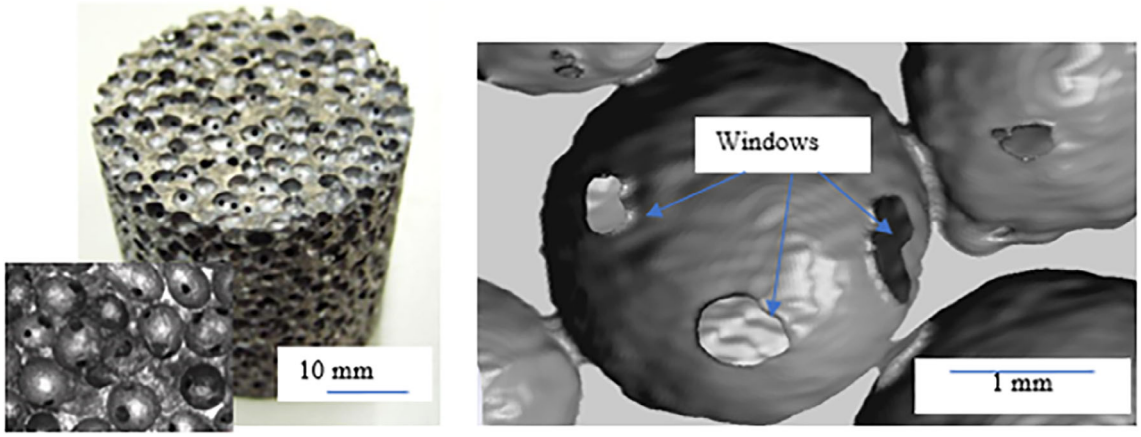

FIGURE 1 An optical micrograph left of a porous sample made by vacuum casting using near-spherical NaCl and right, an X-Ray CT (μCT) image showing the typical pore connectivity (Adapted from References 9, 11 [Color figure can be viewed at wileyonlinelibrary.com]

dominates,[15,16] and the pressure-drop-flow velocity relationship is described only by the Hazen–Darcy Equation;

$$\nabla p = \frac{\mu}{k_o} v_s = \frac{\mu}{k_o} v_p \varepsilon \tag{2}$$

Equation 2 is reportedly[17-20] valid for very slow-flowing fluid in porous media and has been used in a wide range of applications specific to transport in porous media in the past 150 years. Analogous research works involving fluid flow in packed structures (varying in particle sizes, interstices and packing density[21-23] have been tailored toward understanding the relationship between fluid flow velocity and pressure drop developed across porous structures. A significant part of these works has seen the utilization of the pressure–velocity data and fluid flow properties in estimating the permeability of the porous medium using the above expressions. Despite the unique and combined characteristics of high pore volume, high surface area and different pore topologies offered by porous metals over packed beds,[1,12] applicable theories in the use of the above expressions to reliably describe fluid flow behavior in porous metallic structures exist.[24-33]

Understanding the influence of the pore-structure related properties (porosity, pore diameter sizes, pore openings, and specific surfaces) on the permeability of these structures (Figure 1) is important in the design of self-supporting porous materials suitable for engineering and industrial applications of porous metals involving fluid flow. A simple and combined analytical model developed by Despois and Mortensen[29] and Furman et al[30] substantiated the permeability of the "bottleneck-type" structures at Darcy regime which greatly depends on the openings connecting the pores of this unique porous structure. For laminar flow experimental measurements of fluid conducted on microcellular "bottleneck" aluminium foam structures (pore volume fractions from 0.66 to 0.86 and nominal pore size between 108 and 425 μm) made by replication-casting processes, the permeability predicting theoretical "bottleneck" was extended to model flow beyond Darcy[31] and to show that permeability (k_0), Form drag (C), and dimensionless Forchheimer coefficient (C_F) terms in the Darcy–Dupuit–Forchheimer model (Equation 1) are preferentially influenced by the openings (connectivity) than pore diameter sizes. Computational fluid dynamics (CFDs)modeling and simulation of airflow across microcellular structures via tomography datasets in the Forchheimer regime have also been reported in the literature[2] with reasonable fits to experimental data. Figure 2a presents close agreements between experimentally measured and CFD modeled data[2] for samples of similar pore sizes (2.0–2.5) but differentiated by their applied differential pressures during casting; showing a varying degree in the sizes of their pore diameter openings. Table 1 presents these changes in pore-structure related properties and flow information in the inertial dominated flow. Though, currently computed values of flow permeability of these structures in the Darcy regime are also presented in Table 1 and would be discussed later. More so, combination of 3D advanced imaging tools and CFD modeling approach in reported in Otaru et al.[2] was extended to model the pore-structure related properties and flow information of "structural-adapted" bottleneck-structures (Figure 2b). This enabled comprehensive understanding and an appreciation of the changes in pressure drop developed across these materials attributed to the changes in their pore structure-related properties within the Forchheimer dominated regime.

Analogous research works on fluid flow applications of porous metallic components are tailored toward highly porous structures characterized by tetrahedron-like morphology and less emphasis on bottleneck-type structures. Therefore, very little flow predicting Equations are available in the literature for these types of structures. Previously published research article reportedly[9] combined modeling procedure employing packed beds of spherical structures (or discrete element modeling [DEM]) and pore-level CFD provides a virtual and economical way of characterizing the pore-structure related properties of these "bottleneck-dominated" porous structures. Supportable agreements between flow permeability of DEM/CFD data in Reference 9, experimental measurements[32] and established models[30] were substantiated. However, the models in Reference 30 failed to reliably quantify the flow permeability characterized by "bottleneck"

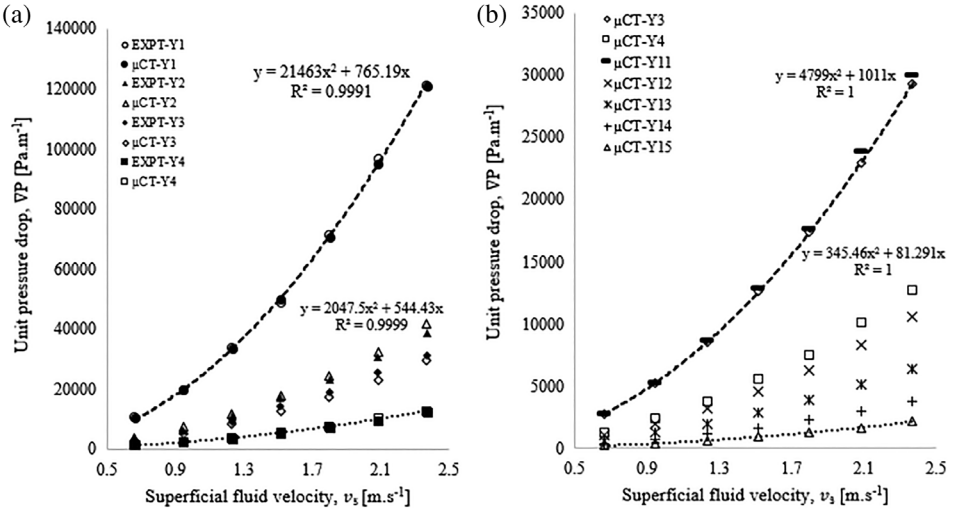

FIGURE 2 Plots of (a) measured (EXPT) and X-ray CT modeled (μCT) pressure drop per unit thickness against superficial air inlet velocity at Forchheimer flow regime (Adapted from Reference 2) and (b) Plots of simulated pressure drop per unit length for semivirtual structures (structural domain erosion, 1–5 pixel removed) using CT images compared with simulations for near-equivalent "real" samples (Y3 and Y4)

TABLE 1 Pore-structure related properties and fluid flow information of porous structures via tomography datasets

Pore-structure related properties						Flow information			
CT sample	ε (%)	*Dw* (mm)	*Dp* (mm)	σ_{FF} (m^{-1})	σ_{FB} (m^{-1})	$k_0/10^{-09}$ (m^2) Darcy	$k_F/10^{-09}$ (m^2) Forchheimer	*C* (m^{-1})	C_F (–)
μCT-Y1	70.80	0.69	2.23	6,413.09	2,649.08	11.1	13.90	17,583.26	2.07
μCT-Y2	72.56	0.72	2.22	6,648.08	2,528.00	13.9	17.08	5,801.76	0.76
μCT-Y3	75.21	0.74	2.27	7,312.92	2,410.80	15.6	18.00	3,985.55	0.53
μCT-Y4	78.40	0.90	2.23	7,455.44	2054.44	28.33	33.40	1,700.52	0.31

Note: *Dp* is the mean pore size (mm), *Dw* is the mean pore openings (mm), ε is the porosity (%), σ_{FB} is the structure surface area per unit bulk volume (m^{-1}), σ_{FF} is the structure surface area per unit structure volume (m^{-1}), k_0 is the Darcian permeability (m^2), k_F is the Forchheimer permeability (m^2), *C* is the Form Drag (m^{-1}), and C_F is the Forchheimer coefficient [–]. Adapted from Reference 2 excluding the flow permeability values at Darcy regime.

structures of lower capillary radius, typically, below 20 μm and this was reportedly attributed in Reference 9 to be the negligible influence of capillary radius on the predictive coordination numbers in the model. This work, therefore, considers CFD modeling and simulations of air pressure drop across these structures in the Darcy regime, typified by pore-diameter Reynolds number (R_{ED}) below unity. This could provide insights into the distinction between the fluid flow behavior of these structures at viscous and inertial dominated regimes and useful in finding a correlation between permeability as a test function of pore-structure related properties of the materials.

2 | RESEARCH APPROACH

The modeling approach used herein is similar to that employed in Reference 2 using the same microcellular structures produced by replication casting technique. In brief, porous metallic structures were produced by infiltrating liquid melts (consisting of 99.5% aluminium at 800°C) into hollow packed beds of near-spherical sodium chloride salts and solidify after mixing before compaction at desired infiltration pressure. Preheating of the bulk of space holders or beads was employed for a temperature range 450 to 600°C to avoid premature solidification of the melt. The foam with salt (occupying its pore space) was then machined in a super-precision Gamet bearing lathe machine to get the desired shape and sizes and was later sintered by dissolution in a warm (40°C) water incubation bath for 72 hours to leave porosity. The size of the pores was reportedly[1] dictated by the size of the salts used (2.0–2.5 mm) while the pore volume and pore openings are largely dictated by controlled packing density and applied differential used to drive the liquid melts into the voids left by the packed beds respectively. Figure 1 clearly presents the microcellular structures ("bottleneck" as they are referred in References 2, 9 showing typical pore diameter sizes, 2.0–2.5 mm, pore diameter openings, 180 μm, and pore volume fraction, 0.64.[13]

A Zeiss Xradia Versa XRM-500 3D X-ray CT microscopy system was used to acquire computer tomography datasets of the "real" samples (Table 1) with voxel dimension of 26 μm resolution in the *x*, *y*, and *z* planes. A three-dimensional advanced image tool (ScanIP) was used for 3D reconstruction of a workable representative volume element (3D RVE CT) extracted from the center of the "real" sample. The size of the computed RVE was ×4–5 the mean pore diameter sizes with porosity differing by ±2 when compared to the "real" samples that are four times longer than the representative sample. Changes to the microstructural properties of the samples were done through sensible creation of "semivirtual" RVE CT structures from the "real" ones using the erosion (removing pixel elements from the frame) tool of the

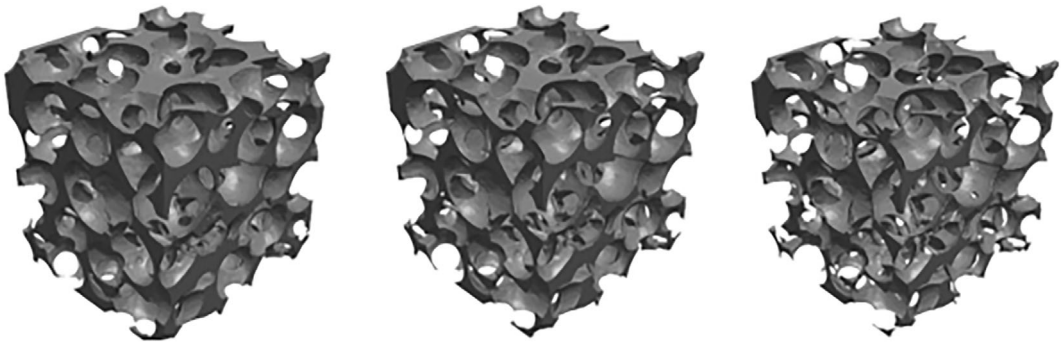

FIGURE 3 Three-dimensional (3D) CT RVE skeletal phases (bottom) for lowest porosity structure, Y1 (left) and after structural erosion of 1- (center, Y11) and 2- (right, Y12) pixels removed from the skeletal phase for 8.5 mm flow thickness

advanced imaging software. This process simply creates a highly porous structure characterized by large pore sizes and wider pores openings as shown by Figure 2 below. Smart mask smoothing was considered over Gaussian smoothing as it preserves accurately the structural information of the materials and an optimized linear tetrahedral mesh was resolved in +FE module of Simpleware™ with mesh density ranging between 2.0 and 2.5 Mcells. The incompressible Stokes flow (or Creeping flow) Equation in the CFD module of COMSOL Multiphysics 5.2™ was solved by simply neglecting the inertial term in the complete Navier–Stokes Equation. This is imperative due to the consideration of very slow fluid flow (0--7×10^{-03}m·s^{-1}) in this study. The creeping flow Equation is given below (Equation 3) as a test function of fluid density (ρ), superficial fluid velocity (v_s), and time (t) and is reportedly[1,9] valid for flowing fluid characterized by small advective inertial terms (viscous dominated flow). A pore fluid inlet velocity ($v_p = v_s/\varepsilon$), zero pressure outlet ($p = 0$), no-slip or walls ($v_p = 0$) on the near-spherical frame (dictated by the shape of the salt beds used during casting of real samples in References 1, 2 and symmetrical boundary conditions ($n.v_p = 0$) on the side faces were considered before solving. It is noteworthy to understand that the meshed fluid domain representative volume was imported into CFD packages by simply inverting the frame (Figure 3) using the Boolean inversion tool in the 3D advanced imaging software

$$\frac{\partial \rho}{\partial t} + \nabla.(\rho v_s) = 0 \tag{3}$$

3 | RESULTS AND DISCUSSION

Figure 4 presents two-dimensional (YZ) sections of the actual 3D velocity (top) and pressure (bottom) profile plots for the "real" (left) and eroded (right) structures. These images are taken to clearly understand the flow behavior of these "bottleneck" structures at Darcy regime (R_{ED} of 0.5 and 0.57, respectively). Fluid flow from top to bottom (indicated by arrows) are observed for connected pores and the intensity of the color scale (values presented in the legends) is largely dependent on the "window" sizes and contacts made by connecting pores.[9,13] The tendency of constrictive response is higher for the "real" (Y1) than the eroded (Y13) structure which can be largely attributed to the smaller pore connectivity of the "real" structures resulting in fewer number of connected pores thereby providing a greater restriction to flowing fluid and higher pressure drop developed across the structure as shown by Figure 4. Fluid flow across these types of highly constricted structures is similar to the ones presented in Reference 30 while that of the less distorted or eroded structures is similar to the highly porous structures reported in Reference 31. This fluid flow behavior cannot be likened to transport in packed beds where the flow of fluid is largely dictated by the packing density of the beds[21,22] but largely attributed to the openings between connected pores within the porous metallic matrices.

Figure 5 (top) presents CFD computed unit pressure drop data developed across the "real" CT structures (a) and an extension to the "semivirtual" structures (b) created by removing 1–5 pixel elements (Y1–Y15) from structural phases of the material with the lowest pore volume (Y1) as presented in Table 1. Table 2 presents the pore structure-related properties (porosity [ε], mean pore diameter openings [Dw], mean pore diameter size [Dp], and specific surfaces [σ_{FF} and σ_{FB}]) and computed flow permeability [k_0] of the porous structures at the Darcy regime. Figure 5, top shows a linear relationship between unit pressure drop developed across all the samples and superficial fluid velocity. The linear relation between velocity and developed unit pressure drop observed for all the samples could be attributed to the neglected inertial effects during CFD modeling and simulation setup. This inertial term is reportedly[1,2,14,31] prevalent for high fluid velocity, typically, in the Forchheimer and Turbulent regimes or fluid flow characterized by the formation of an unsteady pattern of eddies (recirculation effect)[34] resulting in increasing Form drag between the moving fluid and the pore walls. This inertial term should be accounted for in order to completely describe the unit pressure drop developed across high fluid velocity in porous materials.[27] The linear relation for computed pressure drop and velocity for the slow fluid can be attributed to the viscous-dominated forces resulting in the negligible movement of fluid in the normal direction close to the pore

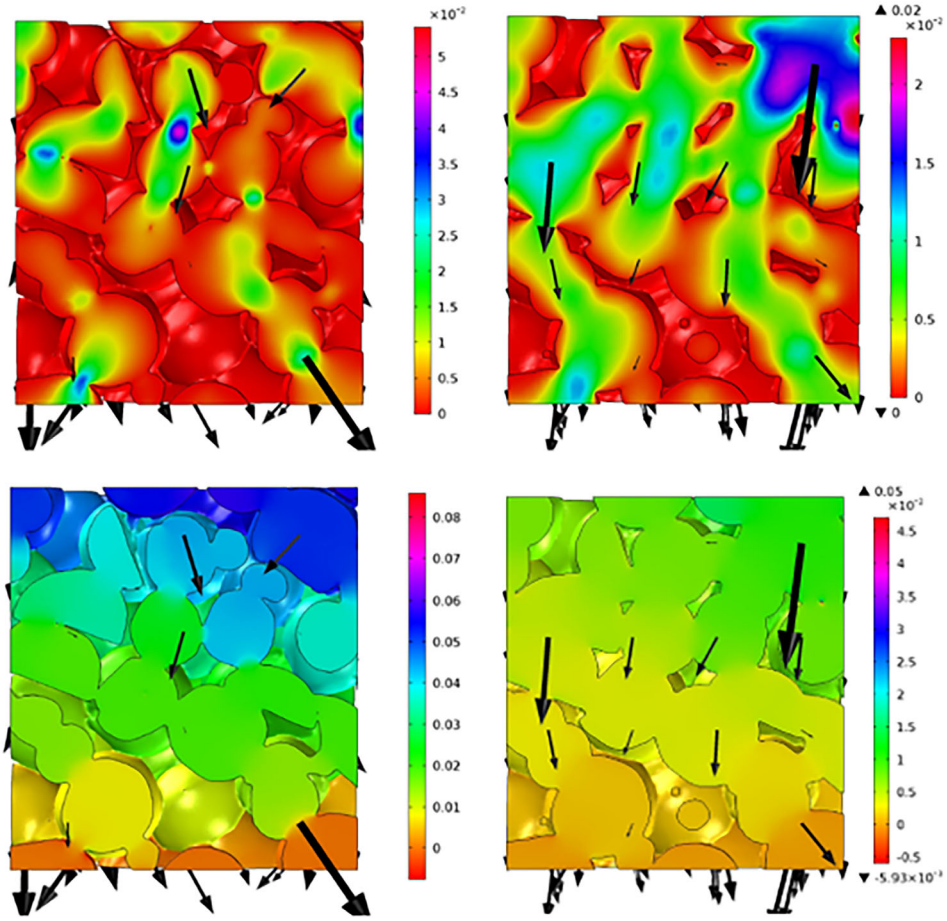

FIGURE 4 Two-dimensional (2D) sections of the velocity (top, [m·s^{-1}]) and pressure drop (bottom, [Pa]) distribution for flow through porous samples Y1 (left) and Y13 (right) microstructures computed for a superficial air inlet velocity of 3.39×10^{-3} m·s^{-1} [Color figure can be viewed at wileyonlinelibrary.com]

walls. Visible streamlines within the pore network of these materials are observably stable and steady with strong tendency toward symmetry for the less distorted or highly porous structures.

For this Darcy regime flow of fluid, the pressure drop is highest for the sample with the lowest pore openings (Y1) and lowest for the sample with the highest pore openings (Y4), as shown by Figure 5a. Figure 5b also demonstrates the rationalization of the "structural-adapted" materials to account for the flow behavior in the "real" samples. For example, the pressure drop developed across the "real" Y3 and Y4 structures are slightly higher than that of the adapted Y11 and Y12 structures, respectively. This can be attributed to the slightly lower pore structure-related properties characterized by the "real" samples thereby resulting in a slight difference in their permeability values as shown in Table 2. Similarly, the unit pressure drops developed across the "semivirtual" structures consistently decrease with increasing pore volume (the removal of pixel elements from the skeletal phases) as shown by Figure 5b. With a superficial inlet velocity of 3.39×10^{-3} m·s^{-1}, the pore fluid velocity decreases from 4.79×10^{-3} to 3.91×10^{-3} m s^{-1} while the unit pressure drop decreases from 5.56 to 0.39 Pa from the "real" (Y1) to the highly eroded structures (Y15). This shows an inverse relationship between the materials pore volume and pressure drop developed across them and would have an overall influence on the permeability of the porous structures. Figure 5 (bottom) shows that the influence imposed by the material pore volume and pore openings on their flow permeability can be described by a nearly perfect direct power-law relation; thereby indicating the contributory effects of the adapted structures to justify this behavior.

The modeling approach used in this study showed that lower pressure drops are obtained for the "adapted" structures while higher pressure drops are obtained for the "real" samples. For every pixel (voxel) element removed, the mean pore diameter size and mean pore openings consistently increased by less than 3% and more than 20%, respectively, indicating a strong dependence of the flow permeability on the pore diameter openings of the materials. Table 2 shows that the permeability of the porous structures is lowest for the "real" samples with the mean openings of 690 μm and highest for the highly eroded structures characterized by mean pore openings of 1,570 μm. As the mean pore diameter openings increase, the materials surface area to bulk volume ratio (σ_{FB}) progressively decreases and the results are the creation of more permeable structures which invariably provide lesser resistance to the flowing fluid across the interstices of the porous media. More so, an increase in the additional pressure drop was observed with increasing pore-nonuniformity (increase in dynamic tortuosity) of the porous materials and this confirms the tendency to increase the energy dissipated within the narrow passages due to the frictional contact between the moving fluid and rigid pore walls.[36-39] However, this was done by a preliminary modeling of the

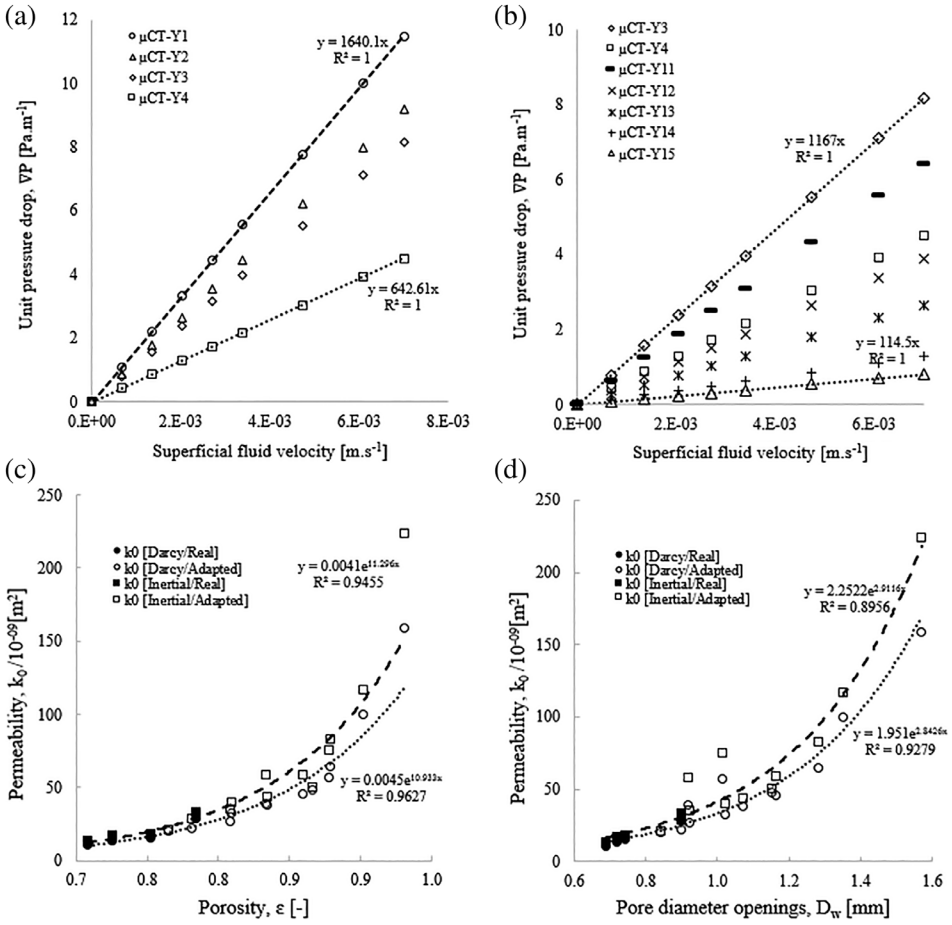

FIGURE 5 X-ray CT modeled (µCT) pressure drop per unit thickness against superficial air inlet velocity at Darcy flow regime for the (A) real and (B) adapted samples. The influence of (C) porosity and (B) pore diameter openings on the permeability of the microcellular structures. The Forchheimer or inertial term permeability values are sourced from Reference 2

Pore-structure related properties						Darcy
CT sample	ε (%)	*Dw* (mm)	*Dp* (mm)	σ_{FF} (m^{-1})	σ_{FB} (m^{-1})	$k_0/10^{-09}$ (m^2)
µCT-Y1	70.80	0.69	2.23	6,413.09	2,649.08	11.10
µCT-Y11	76.52	0.84	2.29	7,351.45	2,214.70	19.90
µCT-Y12	80.88	1.02	2.36	8,031.83	1853.30	32.80
µCT-Y13	86.59	1.15	2.43	8,581.19	1,564.39	48.00
µCT-Y14	90.19	1.35	2.48	9,776.44	1,062.27	99.90
µCT-Y15	93.03	1.57	2.55	10,567.74	791.27	159.00

TABLE 2 Pore-structure related properties and fluid flow information for the adapted porous structures

Note: Y11, Y12, Y13, Y14, and Y15 are symbols for the adapted structures created by removing 1, 2, 3, 4, and 5 voxels from the skeletal phases of the materials, respectively. *Dp* is the mean pore size (mm), *Dw* is the mean pore openings (mm), ε is the porosity (%), σ_{FB} is the structure surface area per unit bulk volume (m^{-1}), σ_{FF} is the structure surface area per unit structure volume (m^{-1}), k_0 is the Darcian permeability (m^2).

CFD pressure drop across longer and shorter length samples and would require additional experimental analysis to affirm the reliability of this hypothesis. It is noteworthy to understand that the permeabilities of these structures were calculated by fitting the superficial fluid velocity and the CFD computed unit pressure drop developed across the samples into Equation (2).

An analytical relationship between the pore-structure related properties and permeability of the "bottleneck-type" porous structures was made possible through the application of dimensionless analysis. Figure 6a shows a near-perfect linear ($R^2 \geq .95$) relationship between Darcian (current) and Forchheimer[2] permeability values against the mean pore openings to pore size ratio using data obtained from the combined "real CT" and "semivirtual" RVE CT samples. For both the "real" and "adapted" samples, the Forchheimer permeability values were consistently higher than flow permeability in the Darcy regime. This difference can be attributed to the contributory effects of the flow velocity arising from the normal and tangential shear stresses at the scale of the boundary walls resulting in the full

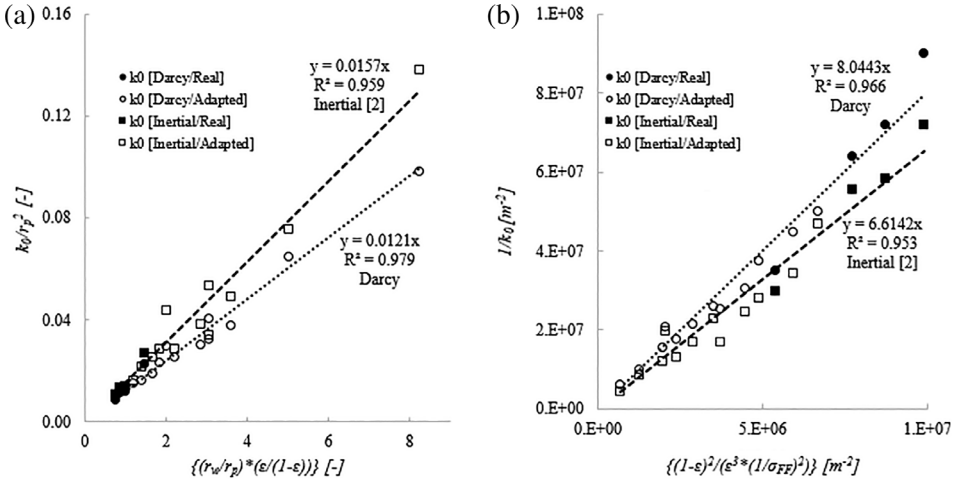

FIGURE 6 Plots of (a) dimensionless reduced permeability (k_0/r_p^2) against reduced pore diameter openings [$(r_w/r_p)*(\varepsilon/(1-\varepsilon))$] and (b) inverse of permeability ($1/k_0$) against the inverse of specific surface [$(1-\varepsilon)^2/(\varepsilon^3*(1/\sigma_{FF})^2)$]

exploration of the geometrical architecture of the materials at higher flow velocity. At Darcy regime, the contributory effect of the normal shear stress is zero or negligible[34,35] and the adjustment in pressure that drives the flow is largely dictated by the instantaneous change in the input flow velocity and variation in the pore diameter openings of these materials. Figure 6a quantifies this difference by empirical constants (W_1^*) of 0.0121 and 0.0157 for both the Darcian and Forchheimer permeabilities.

Analogous work in Reference 40 points out that the well-known Ergun Equation used for predicting flow through porous structures contains a relatable practical relationship between viscous and inertial terms and the porosity of the materials. Whilst, the Ergun Equation was said to accurately predict the pressure drop developed for flowing fluid across packed beds,[41-44] the direct application of similar model does not accurately predict the pressure drops characterized by porous metallic structures.[28] A linear dependence of the permeability against the reduced specific surface was observed in Figure 6b giving empirical constants (W_2^*) of 8.04 and 6.42 for flow in Darcy and Forchheimer regime, respectively. A similar relationship was used for experimentally measured pore-structure related properties and flow permeability of 10-40PPI Duocel foam in Reference 45 giving a direct power-law relationship with 88% correlation factor. This difference may be attributed to the obvious difference in the structural topologies of the materials. Whilst the "bottleneck" structures are characterized by near-spherical pore walls and circular openings, the morphology of the Duocel foams is similar to Kelvin's representation of unit cell (a polygon with eight nonplanar hexagons of no net curvature and six planar quadrilateral faces). This affirms that owing to the complexities of porous metallic structures, a model predicting the flow permeability of the structures may vary for structures of different morphological features and a generalized flow permeability predicting model may require more than bottleneck structures for study.

It is noteworthy to understand that the work presented herein only provide an extension to experimental measurement and CFD modeling works reported in References 1, 2. Analysis of experimentally measured and CFD modeled permeability values reported in Reference 2 are observably close with very little deviations ($R^2 \geq 98\%$) for all porous samples. However, establishing CFD modelling confidence for this work was done by making a comparison between experimentally measured permeability values of highly (Y1) and least (Y4) pressure infiltrated produced porous metals. The experimentally measured values for these structures performed in a constant head permeameter at very slow velocity ($R_{ED} \leq 1$) are $11.9 \pm 0.9 \times 10^{-09}$ m^2 and $27.7 \pm 0.9 \times 10^{-09}$ m^2, respectively. These values represent a less than 6% negligible difference for both cases when compared with the corresponding CFD modeling values obtained using tomography datasets.

4 | CONCLUSION

Pore-level CFD modeling and simulation of Darcy velocity fluid flow across porous metallic structures typified by large pore circular cells and smaller circular apertures have been presented using high-resolution tomography datasets. A linear dependent relationship was observed between CFD computed unit pressure drop developed across these structures against superficial fluid velocity. The permeability of the porous matrices at this Darcy regime and those for Forchheimer regime in Reference 2 consistently increases with increasing pore volume fraction, pore sizes, and most importantly, their pore diameter openings. The difference between the permeability values at these regimes was attributed to the contributory effects imposed by the flow velocity (normal shear stress) at the scale of the boundary walls during high superficial fluid velocity. The extension to "semivirtual" CT structures adapted from the "real" CT representative structures through structural erosion provides an in-depth understanding of the effects imposed by pore-structure related properties on the flow permeability of the materials. This could be useful in reducing the number of design iterations needed for the processing of enhanced porous matrices for application involving fluid flow.

ACKNOWLEDGMENT

Dr. A.J. would like to acknowledge Prof. A.R. Kennedy (Lancaster University, UK), Prof. H.P. Morvan (Rolls Royce Technology UK),

Dr. Martin Corfield, Dr. Hannah Constatin, Mr. Rory Screaton (The University of Nottingham, UK), The University of Nottingham Dean's Award (UK), Bowers and Wilkins Group (UK), Petroleum Technology Development Fund (Nigeria) and Synopsys- Simpleware Ltd (USA) for the provision of porous metallic structures, tomography datasets, licenses, and technical support.

ORCID

Abdulrazak J. Otaru https://orcid.org/0000-0002-3057-4991

REFERENCES

1. Otaru AJ, Morvan HP, Kennedy AR. Airflow measurement across negatively-infiltration processed porous aluminium structures. *AIChE J*. 2019;65:1355-1364.
2. Otaru AJ, Morvan HP, Kennedy AR. Measurement and simulation of pressure drop across replicated microcellular aluminium in the darcy-forchheimer regime. *Acta Mater*. 2018;149:265-275.
3. Jorges PA, Malcom JC. Recent-trends in porous sound-absorbing materials. *Sound Vib*. 2010;44:12-17.
4. Ashby MF, Tianjin LU. Metal foams: A survey. *Sci China Ser (B)*. 2003; 46((6)):521-530.
5. Zhou J. *Porous metallic materials, advanced structural materials*, ed. e. Winston O. Soboyejo, CRC Press, Taylor & Francis Group, USA, 2006:22.
6. Banhart J, Baumeister J. Deformation characteristics of metal foams. *Mater Sci*. 1998;33:1431-1440.
7. Smith BH, Szyniszewski S, Hajjar JF. Steel foam for structures: a review of applications, manufacturing and material properties. *J Constr Steel*. 2012;71:1-10.
8. Kennedy AR. Porous metals and metal foams made from powders. *Powder Metallurgy*. 2012. Dr.Katsuyoshi Kondoh (Ed.), ISBN: 978-953-51-0071-3, InTech, Available from:http://www.intechopen.com/books/powder-metallurgy/the-manufacture-of-porous-and-cellular-metals-bypowder-metallurgy-processes https://doi.org/10.5772/33060.
9. Otaru AJ, Kennedy AR. The permeability of virtual macroporous structures generated by sphere-packing models: comparison with analytical models. *Scr Mater*. 2016;124:30-33.
10. Ashby MF, Evans A, Kennedy AR. The role of oxidation during compaction on the expansion and stability of al foams made via a pm route. *Adv Eng Mater*. 2006;8:568-570.
11. Otaru AJ, Morvan HP, Kennedy AR. Modelling and optimisation of sound absorption in replicated microcellular metals. *Scr Mater*. 2018b; 150:152-155.
12. Otaru AJ. Review on processing and fluid transport in porous metals with a focus on bottleneck structures. *Met Mater Int*. 2019. https://doi.org/10.1007/s12540-019-00345-9.
13. Langston P, Kennedy AR. Discrete element modelling of the packing of spheres and its application to the structure of porous metals made by infiltration of packed beds of nacl beads. *Powder Technol*. 2014; 268:210-218.
14. Antohe B, Lage JL, Price DC, Weber RM. (1997), Experimental determination of the permeability & inertial coefficients of mechanically compressed aluminium metal layers, *ASME J Fluids Eng*, 1997;11:404–412.
15. Dukhan N, Minjeur CA. A two-permeability approach for assessing flow properties in cellular metals. *J Porous Mater*. 2010;18(2):417-424.
16. Despois JF, Marmottant A, Salvo L, Mortensen A. Influence of the infiltration pressure on the structure & properties of replicated aluminium foams. *Mater Sci Eng A*. 2007;462:68-75.
17. Bear J. *Dynamics of fluids in porous media*. New York: Dover Publications, Inc; 1972:124-130.
18. Dybbs A, Edwards RVA. A New look at porous media fluid mechanics—Darcy to turbulent. In: Bear J, Corapcioglu MY, eds. Fundamentals of Transport Phenomena in Porous Media *Nato ASI Series*; (Series E: Applied Sciences), vol 82. Springer, Dordrecht 1984.
19. Innocentini MDM, Salvini VR, Macedo A, Pandolfelli VC. Prediction of ceramic foams permeability using Ergun's Equation. *Mater Res*. 1999; 2(4):283-289.
20. Innocentini MDM, Lefebvre LP, Meloni RV, Baril E. Influence of sample thickness and measurement set-up on the experimental evaluation of permeability of metallic foams. *J Porous Mater*. 2010;17:491-499.
21. Otaru AJ, Kennedy AR. Investigation of the pressure drop across packed beds of spherical beads: comparison of empirical models with pore-level computational fluid dynamics simulations. *ASME Fluids Eng*. 2019;141:071305-1.
22. Lage JL, Krueger PS, Narasimham A. Protocol for measuring permeability and form coefficient of porous media. *Phys Fluids*. 2005;17: 088101.
23. Innocentini MDM, Faleiros RK, Pisani Jr. R, Thijs I, Luyten J., Mullens S. Permeability of porous gelcast scaffolds for bone tissue engineering, *J Porous Mater*, 2010;17:615–627
24. Reutter O, Smirnova E, Sauerhering J, Angel S, Fend T, Pitz-Paal R. Characterization of air flow through sintered metal foams. *ASME J Fluids Eng*. 2008;130(5):051201.
25. Bonnet JP, Topin F, Tadrist L. Flow laws in metal foams: compressibility and pore size effects. *Trans Porous Med*. 2008;73:149-163.
26. Boomsma K, Poulikakos D. On the effective thermal conductivity of a three-dimensionally structured fluid-saturated metal foam. *Int J Heat Mass Trans*. 2001;44:827-836.
27. Boomsma K, Poulikakos D. The effect of comparison and pore size variations on the liquid flow characteristics in metal foams. *ASME J Fluids Eng*. 2002;124:263-273.
28. Dukhan N. *Metal foams: fundamentals and applications*. Lancaster, PA: DESTECH publication, Inc; 2013:1-310.
29. Despois JF, Mortensen A. Permeability of open-pore microcellular materials. *Acta Mater*. 2005;53:1381-1388.
30. Furman EL, Finkelstein AB, Cherny ML. The permeability of aluminium foams produced by replicated-casting. *Metals*. 2013;3:49-57.
31. Weber L, Ingram D, Guardia S, Athanasiou-Ioannou A, Mortensen A. Fluid flow through replicated microcellular materials in the darcy-forchheimer regime. *Acta Mater*. 2017;126:280-293.
32. Njoku R.. *Unpublished Thesis*. University of Nottingham, United Kingdom; 2014.
33. Li Y, Zhendong L, Han F. Airflow resistance and sound absorption behaviour of open-celled aluminium foams with spherical cells. *Procedia Mater Sci*. 2014;4:87-190.
34. Yakhot V, Orsag S, Thamgam S, Gatski T, Speziale C. Development of turbulence models for shear flows by a double expansion technique. *Phys Fluids: A*. 1992;4:1510-1520.
35. Gatski TB. Constitutive Equations for turbulent flows. *Theor Comp Fluid Dyn*. 2004;18(5):345-369.
36. Champoux Y, Stinson MR. On acoustical models fro sound propagation in rigid frame porous materials and the influence of shape factors. *J Acoust Soc Am*. 1992;92(2):1120-1131.
37. Fourar M, Radilla G, Lenormand R, Moyne C. On the non-linear behavior of a laminar single phase flow through two and three-dimensional porous media. *Adv Water Resour*. 2003;27:p669.
38. Otaru AJ, Muhammad MS, Samuel MB, Olugbenga AG, Gana ME, Corfield MR. Pressure drop in high-density porous metals via tomography datasets. *Met Mater Int*. 2019. https://doi.org/10.1007/s12540-019-00431-y.
39. Otaru AJ. Review on the acoustical properties and characterisation methods of sound absorbing porous structures: a focus on microcellular structures made by a replication casting method. *Met Mater Int*. 2019. https://doi.org/10.1007/s12540-019-00512-y.

40. Tadrist L, Miscevis M, Rahli O, Topin F. About the use of fibrous materials in compact heat exchangers. *Exp Thermal Fluid Sci*. 2004;28:193-199.
41. Ergun S. Fluid flow through packed column. *Chem Eng*. 1952;48: 89-94.
42. Harker JH, Richardson JF, Backhurst JR. *Chem Eng*. Butterworth-Heinemann, Oxford, 2002;2:193-233.
43. Karimian SAM, Straatman AG. CFD study of the hydraulic & thermal behaviour of spherical-void-phase porous materials. *Int J Heat Fluid Flow*. 2008;29:292-305.
44. Liu HL, Hwang HR. Permeability prediction of fibrous porous media with complex 3d architectures. *Comp Part A*. 2012;43: 2030-2038.
45. Dukhan N, Patel P. Eq.uivalent particle diameter and length scale for pressure drop in porous metals. *Exp Thermal Fluid Sci*. 2008; 32:1059-1067.

How to cite this article: Otaru AJ. The permeability of replicated microcellular structures in the Darcy regime. *AIChE J*. 2020;66:e16915. https://doi.org/10.1002/aic.16915